# Damage accumulation and defect relaxation in 4*H*-SiC

Y. Zhang,* F. Gao, W. Jiang, D. E. McCready, and W. J. Weber
*Pacific Northwest National Laboratory, P.O. Box 999, Richland, Washington 99352, USA*
(Received 17 November 2003; revised manuscript received 9 June 2004; published 9 September 2004)

A nonlinear dependence of damage disorder on dose is observed for both Si and C sublattices in 4H-SiC under 2 MeV Au irradiation at 165 K. The relative disorder observed along the $\langle \bar{4}40\bar{3} \rangle$ direction is much higher than that along the $\langle 0001 \rangle$ direction. Molecular dynamics (MD) simulations demonstrate that most interstitial configurations are formed on the Si-C dimer rows that are parallel to the $\langle 0001 \rangle$ direction. As a result, these interstitials are shielded by the Si and C atoms on the lattice sites, which significantly reduces the contribution of these interstitials to the backscattering/reaction yield along the $\langle 0001 \rangle$ direction. During isochronal annealing below room temperature, the relative disorder decreases along the $\langle 0001 \rangle$ direction, as expected; however, the disorder is stable on the Si sublattice and increases slightly on the C sublattice when measured along the $\langle \bar{4}40\bar{3} \rangle$ direction due to relaxation of some metastable defects to lower energy configurations. As the annealing temperature increases, similar recovery behavior on both Si and C sublattices along the $\langle 0001 \rangle$ direction indicates coupling of Si and C recovery processes; however, slightly higher recovery temperatures on the C sublattice along the $\langle \bar{4}40\bar{3} \rangle$ direction suggests some decoupling of the Si and C recovery processes. Based on the structures and energetics of defects from MD simulations, new insights into defect configurations and relaxation processes are described.

DOI: 10.1103/PhysRevB.70.125203 PACS number(s): 61.80.Jh, 61.85.+p, 61.82.−d

## I. INTRODUCTION

The wide band gap semiconductor silicon carbide (SiC) has remarkable physical, chemical and electronic properties[1–3] that make it very attractive for high-speed communications and high-temperature, high-frequency and high-power applications. Ion implantation is the only planar, selective-area doping technique available for SiC, since the diffusion coefficients of impurities in SiC are negligibly small at or below 1800 K.[4,5] Ion implantation, however, inevitably produces a significant concentration of defects and lattice disorder, which lead to a growth of secondary defects or other polytype structures during post-implantation annealing or high temperature operation. The failure of prototype devices, such as high leakage currents, poor and uneven injection during forward bias and premature breakdown under reverse bias,[6,7] are often associated with point defects or larger agglomerates of point defects formed by the implantation process or during post-implantation annealing. One of the critical issues for SiC device fabrication is, therefore, to reduce the effects of implantation-induced damage. Intensive studies[8–16] have been carried out, both experimentally and theoretically, to understand defect production, accumulation and damage annealing mechanisms, which are essential to the implementation of implantation doping techniques in SiC-based electronic device fabrication.

Among a number of polytypes, 4H-SiC is particularly promising because of its wide bandgap and its high electron mobility.[17] The objective of the present work is to study ion-induced damage accumulation, defect relaxation and annihilation following annealing in 4H-SiC using ion channeling techniques along two crystallographic directions. Together with molecular dynamics (MD) simulations, new insights into defect configurations and relaxation are described.

## II. EXPERIMENTAL PROCEDURE

The high purity, epitaxial single crystal film of 4H-SiC used in this study was over 8 $\mu$m thick, grown on a 4H-SiC *n*-type substrate that was obtained from Sterling Semiconductor, Inc (Reston, Virginia). The wafer surface normal was 8° off the $\langle 0001 \rangle$ orientation, and the epitaxial layer was doped with nitrogen in the range of $1.5\times10^{15}$ cm$^{-3}$.

Ion irradiation and the subsequent investigation of damage accumulation and recovery using channeling techniques were carried out using the 3.0 MV electrostatic tandem accelerator facility within the Environmental Molecular Sciences Laboratory (EMSL) at the Pacific Northwest National Laboratory (PNNL). The high-quality 4H-SiC samples were irradiated by 2.0 MeV $Au^{2+}$ ions 60° off the surface normal at 165 K to fluences from $3\times10^{12}$ to $1.5\times10^{13}$ cm$^{-2}$. At each ion fluence, the local dose at the damage peak in displacements per atom (dpa) was determined using the SRIM (stopping and range of ions in matter) 2000 full-cascade simulation code[18] under the assumptions of a sample density of 3.21 g/cm$^3$ and threshold displacement energies of 20 and 35 eV for the C and Si sublattices, respectively.[11] The conversion factor at the damage peak from ion fluence ($10^{14}$ $Au^+$cm$^{-2}$) to dose (dpa) is 0.627 under the current irradiation conditions.

The crystallographic structure of 4H-SiC consists of tetrahedral layers of $SiC_4$ or $CSi_4$, which are perpendicular to the *c*-axis with a stacking sequence of *ABACABAC*… . Figure 1 illustrates a hexagonal structure containing one stacking sequence of the Si sublattice in 4H-SiC, where the C sublattice is not shown to more clearly indicate the directions for the channeling measurements. The plane perpendicular to the *c*-axis is the basal plane, and the lattice constants *a* and *c* are 0.30730 and 1.0053 nm, respectively.[17] In the current

 ©2004 The American Physical Society

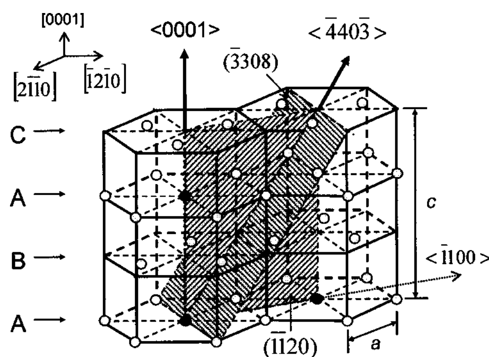


FIG. 1. The first stacking sequence of Si sublattice in 4H-SiC with the axes $\langle 0001 \rangle$ and $\langle \bar{4}40\bar{3} \rangle$ indicated. The filled symbol is used when the Si atom is on the corresponding axis.

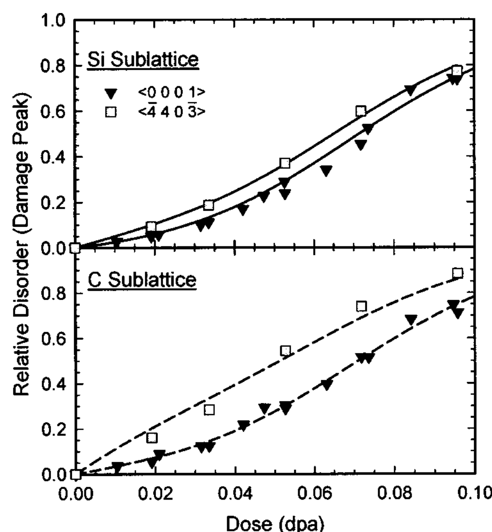


FIG. 2. The relative disorder along the $\langle 0001 \rangle$ and $\langle \bar{4}40\bar{3} \rangle$ directions on both Si (a) and C (b) sublattices as a function of local dose at the damage peak. The lines are the fits of the disorder accumulation model [Eq. (3)] to the data.

study, the relative disorder along the $\langle 0001 \rangle$ ($c$-axis) and the $\langle \bar{4}40\bar{3} \rangle$ directions are measured using channeling techniques. As indicated in Fig. 1, the $\langle \bar{4}40\bar{3} \rangle$ direction, which is the zone axis defined by the $(\bar{1}\bar{1}20)$ and $(\bar{3}308)$ planes, is obtained by tilting the sample 35.3° from the $\langle 0001 \rangle$ direction toward the $\langle \bar{1}100 \rangle$ direction. In the current study, the angle between the probe beam and surface normal is 8° and 27.3° for the $\langle 0001 \rangle$ and $\langle \bar{4}40\bar{3} \rangle$ directions, respectively.

The disorder on both Si and C sublattices in SiC was determined simultaneously from both Rutherford backscattering spectroscopy (RBS) and $^{12}C(d,p)^{13}C$ nuclear reaction analysis (NRA) at a scattering angle of 150° using a 0.94 MeV $D^+$ beam, as reported previously.[8,9] The ion-induced disorder on both Si and C sublattices in the as-implanted samples was measured at 150 K along both $\langle 0001 \rangle$ and $\langle \bar{4}40\bar{3} \rangle$ directions. Isochronal annealing for 20 minutes was performed *in situ* under high vacuum ($10^{-7}$ mbar) in the target chamber at temperatures up to 870 K, where most point defects are mobile. Following each annealing step, the residual disorder on both Si and C sublattices in the annealed samples was also measured along the $\langle 0001 \rangle$ and $\langle \bar{4}40\bar{3} \rangle$ directions by RBS and NRA. For samples that were annealed at 200, 250 and 300 K, the channeling measurements were carried out at 150 K; while for samples annealed at a higher temperature, the analysis was performed at room temperature. This procedure ensured that the thermal recovery processes were quenched prior to analysis.

## III. RESULTS AND DISCUSSION

### A. Disorder accumulation model

Implantation-induced disorder in 4H-SiC, which is measured by the ion channeling techniques, consists of contributions from amorphous material, interstitials and small interstitial clusters. The amorphous fraction can be described well using a direct-impact, defect-stimulated (DI/DS) model,[19] where amorphization occurs directly within a cascade and from defect-stimulated processes at crystalline/amorphous (c/a) interfaces. According to the DI/DS model,[19] the amorphous fraction, $f_a$, is given by

$$f_a = 1 - (\sigma_a + \sigma_s)/\{\sigma_s + \sigma_a \exp[(\sigma_a + \sigma_s)D]\}, \tag{1}$$

where $\sigma_a$ is the amorphization cross section, $\sigma_s$ is the effective cross section for defect-stimulated amorphization, and D is the local dose (dpa).

Ion irradiation also leads to the formation and accumulation of point defects and small defect clusters in the residual crystalline material;[15] however, only interstitials and interstitial clusters contribute measurably to the relative disorder. The corresponding contribution of such defects to the relative disorder, $S_d$, is expressed by[9]

$$S_d = S_d^*[1 - \exp(-BD)](1 - f_a), \tag{2}$$

where $S_d^*$ is the saturation value for the defect-induced disorder, and the parameter B ($\text{dpa}^{-1}$) is proportional to an effective recombination volume for the specific defects giving rise to $S_d$.

The total disorder, $S$, produced under ion-beam irradiation and measured by ion-channeling methods is given by

$$S = f_a + S_d. \tag{3}$$

This disorder accumulation model [Eq. (3)] can be fit to the data obtained at the damage peak by channeling RBS and NRA.

### B. Disorder accumulation

The depth profiles of the relative disorder on the Si and C sublattices due to irradiation were determined from the RBS and NRA spectra using an iterative procedure,[20–22] as in previous studies.[8,9] The relative disorder on the Si and C sublattices at the damage peak for the as-implanted samples is shown in Fig. 2 as a function of the local dose (dpa). A sigmoidal dependence of damage accumulation on dose is observed along both directions and on both sublattices. The lines are model fits of Eq. (3) to the data. The parameters are

TABLE I. The model parameters from the fit of Eq. (3) to the data in Fig. 2.

| | Si⟨0001⟩ | C⟨0001⟩ | Si⟨$\bar{4}40\bar{3}$⟩ | C⟨$\bar{4}40\bar{3}$⟩ |
|---|---|---|---|---|
| $\sigma_a(\mathrm{dpa}^{-1})$ | 2.0 | 2.0 | 2.0 | 2.0 |
| $\sigma_s(\mathrm{dpa}^{-1})$ | 41.8 | 41.5 | 43.6 | 44.0 |
| $S_d^*$ | 0.005 | 0.0167 | 0.118 | 0.403 |
| $B(\mathrm{dpa}^{-1})$ | 100 | 100 | 25 | 25 |

summarized in Table I. The significantly larger values of $\sigma_s$ relative to $\sigma_a$ (Table I) for both directions indicate that defect-stimulated amorphization is the primary mechanism that leads to the growth of amorphous nuclei and coalescence of amorphous domains. The dominance of defect-stimulated amorphization processes has also been confirmed in MD simulations of cascade overlap in 3C-SiC.[14] The cross sections, $\sigma_a$ and $\sigma_s$, are similar for both Si and C sublattices (Table I) and independent of channel orientations, which is expected since the amorphous state is 3-dimensional and essentially stoichiometric (no enrichment in either element).

It is important to note that the disorder along the ⟨$\bar{4}40\bar{3}$⟩ direction, as shown in Fig. 2, is much higher than that along the ⟨0001⟩ direction. The results in Fig. 3, as well as the fitting parameters from Table I, indicate that the higher disorder along the ⟨$\bar{4}40\bar{3}$⟩ direction is due to different contributions from $S_d$, which is primarily from irradiation-induced interstitials in the residual crystalline regions. Furthermore, the relative disorder, $S_d$ in Fig. 3, is larger on the C sublattice than the disorder on the Si sublattice along both directions, which is consistent with the higher displacement production rate for C relative to Si predicted by MD simulations.[11–13] This is further illustrated by the significantly larger values of $S_d^*$ for the C sublattice, as compared with the corresponding

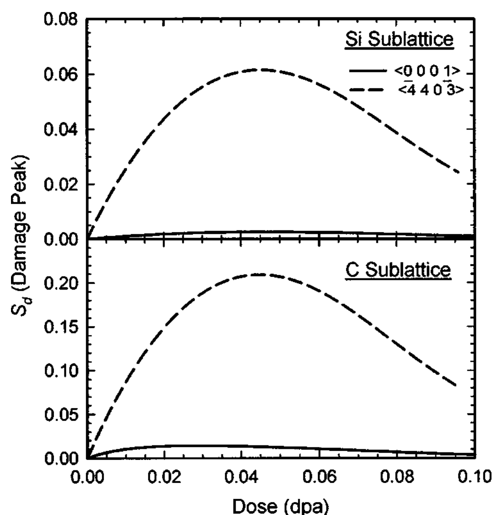


FIG. 3. The fitted relative disorder from irradiation-induced interstitials and small interstitial clusters in the residual crystalline regions, $S_d$, on both Si (a) and C (b) sublattices along the ⟨0001⟩ and ⟨$\bar{4}40\bar{3}$⟩ directions as a function of local dose at the damage peak.

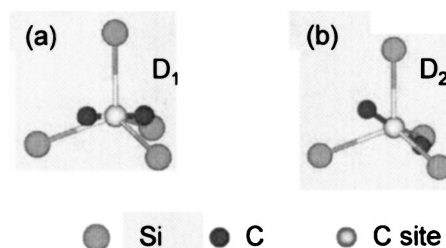


FIG. 4. Fundamental structure of dumbbell interstitials: (a) $D_{1C+C}$ and (b) $D_{2C+C}$.

values for the Si sublattice (Table I). The value of $B$ is related to the effective recombination volume for specific defects. The same $B$ values along the same orientation for the Si and C sublattices is expected, since close-pair recombination kinetics are similar for Si and C.[12] The difference in $B$ and $S_d$ along the different channeling directions can be explained based on an understanding of the irradiation-induced defect configurations in 4H-SiC from MD calculations.[23,24]

### C. Defect configurations

The results of molecular dynamics simulations on defect evolution in 3C-SiC[11–14] under ion irradiation indicate that energetic ions primarily produce interstitials, monovacancies, antisite defects, and small defect clusters within collision cascades. As the channeling techniques are relatively insensitive to vacancies and antisite defects, the discussion on defect configurations based on MD results will focus on interstitial-type defects.

The tetrahedral structure of $SiC_4$ or $CSi_4$, with bond angles of 109.5°, is the basic cell in all SiC polytypes. The higher number of nonequivalent lattice sites in 4H-SiC[23,24] leads to a greater variety of potential elementary defects than in 3C-SiC. In covalent SiC, dumbbell interstitials (two atoms sharing one lattice site) are important defects due to their low formation energies. As shown in Figs. 4(a) and 4(b) and described in more detail elsewhere,[23,24] the dumbbell interstitials can be classified into $D_1$ and $D_2$ groups, where the $D_1$ dumbbell lies in one of the six planes formed by two Si-C bonds, and $D_2$ dumbbells are situated in two perpendicular planes formed by two Si-C bonds. There exist twenty $D_1$ and twelve $D_2$ dumbbell configurations in 4H-SiC. For example, two C interstitials classified as $D_{1C+C}$ and $D_{2C+C}$ are shown in Figs. 4(a) and 4(b), respectively, where the central carbon atom in the tetrahedral position is replaced by a C-C dumbbell.

In addition to dumbbell interstitials, there are fourteen possible single interstitial configurations. In 4H-SiC, the lattice structure can be characterized using Si-C dimer rows (parallel to the c-axis) that are perpendicular to the basal plane, namely long (dashed arrow) and short rows (dotted arrow), as indicated in Fig. 5. There are seven possible positions for interstitials on each sublattice. For example, the seven C interstitial configurations are illustrated in Figs. 6(a)–6(e). There are two C tetrahedral configurations on the long row, as shown in Fig. 6(a), surrounded by four C atoms ($C_{TC}$) or by four Si atoms ($C_{TSi}$). On the three hexagonal

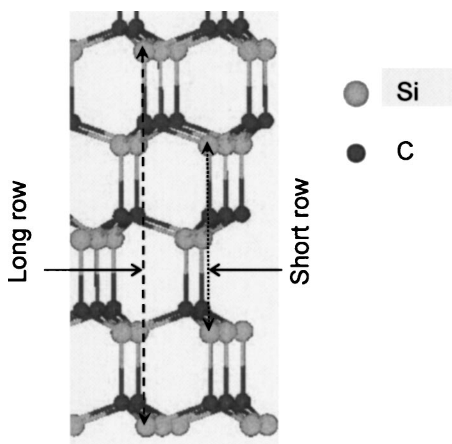


FIG. 5. Details of a dimer sequence of the long row (dashed arrow) and short row (dotted arrow) in 4H-SiC.

positions, there are two possible C interstitial defects ($C_{HC}$ and $C_{HSi}$) on the long row inside the two hexagonal $Si_3C_3$ rings (dotted circles) that are parallel to the basal plane, as shown in Fig. 6(b), and one ($C_H$) inside a hexagonal $Si_3C_3$ ring (dashed circle) that is not parallel to the basal plane, as shown in Fig. 6(c). Furthermore, there exist two highly symmetric interstitial structures: $C_{HR}$ between the two hexagonal $Si_3C_3$ rings (dotted circles) on the long row, as shown in Fig. 6(d), and $C_{TR}$ between trigonal $Si_3$ ring (dashed circle) and trigonal $C_3$ ring (dotted circle) on the short row, as shown in Fig. 6(e). In 4H-SiC, there also exist seven corresponding configurations for single Si interstitials. Based on calculated formation energies,[23,24] all seven C interstitial configurations are stable, but only tetrahedral Si interstitials ($Si_{TSi}$ and $Si_{TC}$) and the Si interstitial between two hexagonal $Si_3C_3$ rings ($Si_{HR}$) are stable. While the other Si configurations ($Si_H$, $Si_{HSi}$, $Si_{HC}$ and $Si_{TR}$) are unstable, such interstitials may be produced by irradiation. Therefore, it can be concluded that most single interstitial defects, except $C_H$ and $Si_H$ produced under irradiation, are located on the Si-C dimer rows that are parallel to the c-axis.

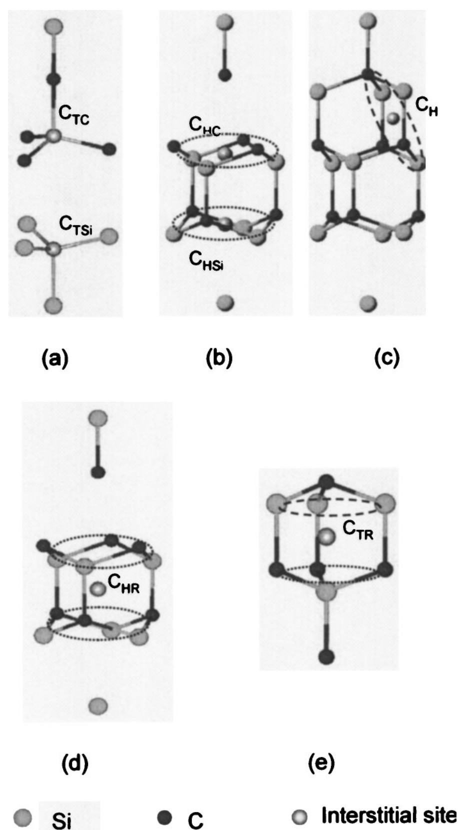


FIG. 6. Seven possible positions for C single interstitials: (a) two tetrahedral positions on the long row, (b) and (c) three hexagonal positions, and two highly symmetric interstitial structures, (d) between the two hexagonal $Si_3C_3$ rings on the long row, and (e) between a trigonal $Si_3$ and a trigonal $C_3$ rings on the short row.

When aligning the probe beam along the $\langle 0001 \rangle$ direction, backscattering contributions from the $D_1$ and $D_2$ dumbbell interstitials and the $C_H$ and $Si_H$ type single interstitials can be observed. The other single interstitial configurations, such as shown in Figs. 6(a), 6(b), 6(d), and 6(e), are shielded from the analysis beam by the Si-C rows along the $\langle 0001 \rangle$ direction, and therefore will not contribute to the backscattering/reaction yield. On the other hand, along the $\langle \bar{4}40\bar{3} \rangle$ direction, all seven possible configurations for the single interstitials on each sublattice and all the dumbbell interstitials are accessible, in varying degrees, to the probe beam. Since all interstitial configurations contribute in some degree to the backscattering along the $\langle \bar{4}40\bar{3} \rangle$ direction, a significantly higher relative disorder is observed on both the Si and C sublattices along this direction; while along the $\langle 0001 \rangle$ direction, only a fraction of the interstitial configurations contribute to the disorder. Multiaxial channeling studies[25] in 6H-SiC under Au irradiation also indicated the presence of stable interstitial configurations at 300 K that are shadowed along the $\langle 0001 \rangle$ direction, which is attributed to similar defect configurations. The different $B$ values along both directions indicate that the effective recombination volume is different for the dumbbell interstitials and the single interstitial configurations. MD simulations[12] indicate that the activation energies for defect recombination in 3C-SiC range from 0.22 to 1.6 eV for C Frenkel pairs and from 0.28 to 0.9 eV for Si Frenkel pairs. The activation energies for recombination of close-pairs with separation distances less than $0.7a$ are between 0.24 to 0.38 eV, and smaller activation energies are normally observed for the dumbbell interstitials.[12] These close-pair recombination energies for 3C-SiC are relevant to the observations for 4H-SiC at 165 K in the current study, and the larger $B$ values along the $\langle 0001 \rangle$ direction are consistent with the generally smaller activation energies for dumbbell interstitials.

### D. Damage recovery

After completion of the channeling measurements for the as-implanted samples, isochronal annealing was carried out sequentially at temperatures from 200 to 870 K. The relative residual disorder for the higher dose samples at the damage peak for both Si and C sublattices was determined along both directions after each annealing, and the results are shown in Fig. 7.

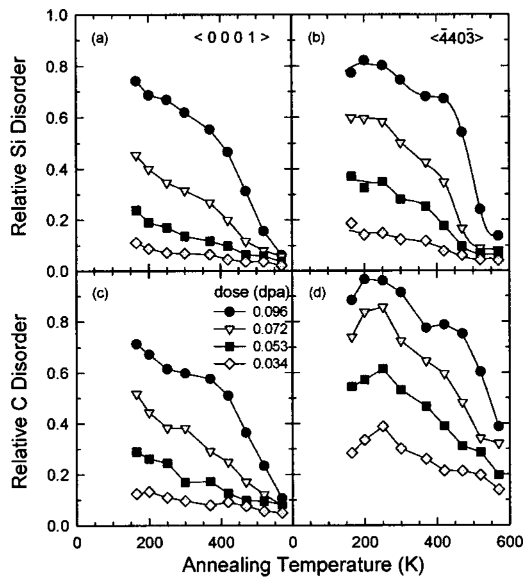


FIG. 7. Isochronal recovery of relative disorder along the ⟨0001⟩ and ⟨$\bar{4}$40$\bar{3}$⟩ directions for both Si and C sublattices at the damage peak in $Au^{2+}$ irradiated 4H-SiC. (a) Si sublattice along the ⟨0001⟩ direction; (b) Si sublattice along the ⟨$\bar{4}$40$\bar{3}$⟩ direction; (c) C sublattice along the the ⟨0001⟩ direction; and (d) C sublattice along the ⟨$\bar{4}$40$\bar{3}$⟩ direction.

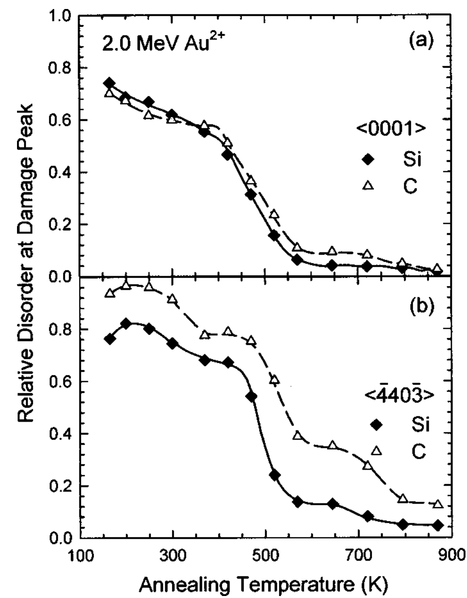


FIG. 8. Isochronal recovery of relative disorder along the (a) ⟨0001⟩ and (b) ⟨$\bar{4}$40$\bar{3}$⟩ directions for both Si and C sublattices at the damage peak in $Au^{2+}$ irradiated 4H-SiC with an ion fluence of $1.5\times10^{13}$ ions $cm^{-2}$ (0.096 dpa at the damage peak).

For annealing below room temperature, distinct annealing behavior is observed along each of the directions. The relative disorder along the ⟨0001⟩ direction decreases as temperature increases, but the relative disorder along the ⟨$\bar{4}$40$\bar{3}$⟩ direction is largely unchanged on the Si sublattice and increases slightly on the C sublattice. Recent MD simulations[12] of defect generation by displacement cascades in SiC have shown that a large portion (~60%) of the interstitials come to rest at distances of less than 0.707*a* (where *a* is the lattice parameter) from the nearest vacancies. The recombination of interstitials with vacancies will lead to a decrease in disorder, as observed along ⟨0001⟩. The exact defect kinetics and mechanisms for the relative increase along the ⟨$\bar{4}$40$\bar{3}$⟩ direction, particularly for the C sublattice, are unclear; however, this behavior must be associated with the relaxation of defects to lower-energy configurations that give rise to an increased contribution to the backscattering. Determining the nature of the defects and processes associated with the relaxation and recovery in this temperature region will require careful experimental studies in parallel with computer simulations, both of which are planned as part of future work.

As the annealing temperature further increases, the residual disorder decreases along both the ⟨0001⟩ and ⟨$\bar{4}$40$\bar{3}$⟩ directions, as shown in Fig. 7. At higher annealing temperatures (above room temperature), interstitials will migrate, resulting in annihilation or clustering. This leads to a decrease in the concentration of local defects and some defect-stimulated epitaxial recrystallization of amorphous domains, both of which will result in decreased local disorder. Above room temperature, there are recovery stages at ~300 and 500 K that are more pronounced for the high-dose samples. The recovery stage at ~500 K occurs for both Si and C sublattices and is consistent with the general recovery behavior observed in SiC irradiated with He,[26] Al,[9] and Xe.[27] This recovery stage is not observed by positron lifetime spectroscopy,[28] which suggests that vacancy defects are unaffected by the recovery process at these temperatures.

Although recovery depends on the initial defect configurations, disorder level and sublattice, similar recovery behavior above room temperature on both Si and C sublattices is observed along the ⟨0001⟩ direction. The recovery behavior of the highest dose sample along both directions is shown over a wider temperature range in Fig. 8. The results in Figs. 7 and 8 suggest similar defect migration energies or that the defect migration and annihilation processes on the two sublattices along the ⟨0001⟩ direction are coupled. Recent *ab initio* calculations[16] of stable defect configurations in 3C-SiC indicate that C-C and C-Si split interstitials are the most stable configurations for the C interstitials. Furthermore, recent MD simulations[29] indicate that the long-range migration of interstitials occurs by hopping from sublattice to sublattice. Thus, the coupled recovery processes observed on the Si and C sublattices is partially associated with C interstitial migration. MD simulations[11–13] have also indicated that significant anti-site defects are produced on both sublattices in SiC by energetic collision cascades, and the recovery of the anti-site defects may also lead to coupled recovery processes on the Si and C sublattices.

While similar recovery behavior is observed for Si and C along the ⟨0001⟩ direction, the recovery behavior on the Si and C sublattices is markedly different along the ⟨$\bar{4}$40$\bar{3}$⟩ direction. As shown in Fig. 8, a recovery stage at ~700 K is observed, which is much more pronounced along the ⟨$\bar{4}$40$\bar{3}$⟩ direction. Although more damage is annealed in the recovery

stage at $\sim$500 K than at the higher temperature stage ($\sim$700 K), the relative amount of recovery within the two stages is clearly discernable between the Si and C sublattices along the $\langle\bar{4}40\bar{3}\rangle$ direction. For the Si sublattice, nearly 50% of the irradiation-induced disorder recovers along the $\langle\bar{4}40\bar{3}\rangle$ direction between $\sim$400 and 600 K, while another 10% of the original Si disorder recovers at temperatures between $\sim$650 and 800 K. For the C sublattice, about 40% of the irradiation-induced disorder recovers the $\langle\bar{4}40\bar{3}\rangle$ direction between 400 and 600 K, and $\sim$20% of the original C disorder recovers between 650 and 800 K. The recovery on the C sublattice appears to be slightly shifted to higher temperatures. The different recovery behavior of the Si and C sublattices along the $\langle\bar{4}40\bar{3}\rangle$ direction may suggest some decoupling of the Si and C recovery processes. Since most single interstitials along the Si-C dimer rows are detectible along the $\langle\bar{4}40\bar{3}\rangle$ direction rather than the $\langle 0001\rangle$ direction, the decoupling of the Si and C recovery processes may mostly be associated with the recovery of single interstitial configurations.

Complete recovery of the residual disorder is not observed on either sublattice or along either direction after annealing up to 870 K due to residual amorphous domains and stable defect clusters. Thermal annealing at 1300 K or higher is necessary for complete restoration of the crystalline order.[30]

## IV. CONCLUSIONS

Damage accumulation on both Si and C sublattices shows sigmoidal dependence on dose under Au irradiation at 165 K. The nonlinear behavior is described well by a disorder accumulation model, which indicates that defect-stimulated amorphization is the primary amorphization mechanism. The observed relative disorder along the $\langle\bar{4}40\bar{3}\rangle$ direction is much higher than that along the $\langle 0001\rangle$ direction. Based on MD simulations of stable defect configuration, all dumbbell interstitials and single interstitial configurations are detectable along the $\langle\bar{4}40\bar{3}\rangle$ direction. Since most single interstitial configurations are formed on the Si-C dimer rows that are parallel to the $\langle 0001\rangle$ direction, these interstitials are shielded by the Si and C atoms on the lattice sites, which significantly reduces the backscattering/reaction yield along the $\langle 0001\rangle$ direction. During isochronal annealing below room temperature, the relative disorder decreases along the $\langle 0001\rangle$ direction but increases slightly along the $\langle\bar{4}40\bar{3}\rangle$ direction due to different relaxation and recovery processes for interstitial defects and anti-site defects. As the annealing temperature increases up to 870 K, similar recovery behavior on both Si and C sublattices along the $\langle 0001\rangle$ direction suggests coupling of recovery processes of Si and C defects; however a slight shift to higher temperature of recovery on the C sublattice along the $\langle\bar{4}40\bar{3}\rangle$ direction may indicate some decoupling of the Si and C recovery processes. A recovery stage at $\sim$500 K for the Si and C sublattices is attributed to increased mobility of interstitial defects.

## ACKNOWLEDGMENT

The authors are grateful to Dr. A. Hallén from the Royal Institute of Technology, Sweden for providing the 4H-SiC wafer. This work was supported by the Division of Materials Sciences and Engineering, the Office of Basic Energy Sciences, U.S. Department of Energy. The operational support for the EMSL accelerator was provided by the Office of Biological and Environmental Research, U.S. Department of Energy. Pacific Northwest National Laboratory is operated by Battelle for the U.S. Department of Energy under Contract No. DE-AC06-76RLO 1830.

*Corresponding author. Email address: Yanwen.Zhang@pnl.gov

[1] W. Wesch, Nucl. Instrum. Methods Phys. Res. B **116**, 305 (1996).
[2] J. B. Casady and R. W. Johnson, Solid-State Electron. **39**, 1409 (1996).
[3] C. Raynaud, J. Non-Cryst. Solids **280**, 1 (2001).
[4] T. Kimoto, A. Itoh, H. Matsunami, T. Nakata, and M. Watanabe, J. Electron. Mater. **24**, 235 (1995).
[5] J. Senzaki, K. Fukuda, S. Imai, Y. Tanaka, N. Koboyashi, H. Tanoue, H. Okushi, and K. Arai, Appl. Surf. Sci. **159-160**, 544 (2000).
[6] H. Lendenmann, F. Dahlquist, J. P. Bergman, H. Bleichner, and C. Hallin, Mater. Sci. Forum **389-393**, 1259 (2002).
[7] D. T. Morisette and J. A. Cooper, Jr., Mater. Sci. Forum **389-393**, 1133 (2002).
[8] Y. Zhang, W. J. Weber, W. Jiang, C. M. Wang, A. Hallén, and G. Possnert, J. Appl. Phys. **93**, 1954 (2003).
[9] Y. Zhang, W. J. Weber, W. Jiang, A. Hallén, and G. Possnert, J. Appl. Phys. **91**, 6388 (2002).
[10] L. Henry, M.-F. Barthe, C. Corbel, P. Desgardin, G. Blondiaux, S. Arpiainen, and L. Liszkay, Phys. Rev. B **67**, 115210 (2003).
[11] R. Devanathan, W. J. Weber, and F. Gao, J. Appl. Phys. **90**, 2303 (2001).
[12] F. Gao, and W. J. Weber, J. Appl. Phys. **94**, 4348 (2003).
[13] F. Gao and W. J. Weber, Phys. Rev. B **63**, 054101 (2001).
[14] F. Gao and W. J. Weber, Nucl. Instrum. Methods Phys. Res. B **207**, 10 (2003).
[15] F. Gao and W. J. Weber, Phys. Rev. B **66**, 024106 (2002).
[16] F. Gao, E. J. Bylaska, W. J. Weber, and L. R. Corrales, Phys. Rev. B **64**, 245208 (2001).
[17] M. E. Levinshtein, S. L. Rumyantsev, and M. S. Shur, Editors, *Properties of Advanced Semiconductor Materials: GaN, AlN, InN, BN, SiC, and SiGe* (Wiley and Sons, New York, 2001).
[18] J. F. Ziegler, J. P. Biersack, and U. Littmark, *The Stopping and Range of Ions in Solids* (Pergamon, New York, 1985).
[19] W. J. Weber, Nucl. Instrum. Methods Phys. Res. B **166-167**, 98 (2000).

[20] L. C. Feldman, J. W. Mayer, and S. T. Picraux, *Materials Analysis by Ion Channeling* (Academic, New York, 1982), p. 117.
[21] M. L. Swanson, in *Handbook of Modern Ion Beam Materials Analysis*, edited by J. R. Tesmer and M. Nastasi (Materials Research Society, Pittsburgh, PA, 1995), p. 263.
[22] J. S. Williams and R. G. Elliman, in *Ion Beams for Materials Analysis*, edited by J. R. Bird and J. S. Williams (Academic, Australia, 1989), p. 286.
[23] F. Gao, M. Posselt, V. Belko, Y. Zhang, and W. J. Weber, Nucl. Instrum. Methods Phys. Res. B **218**, 74 (2004).
[24] M. Posselt, F. Gao, W. J. Weber, and V. Belko, J. Phys.: Condens. Matter **16**, 1307 (2004).
[25] W. Jiang and W. J. Weber, Phys. Rev. B **64**, 125206 (2001).
[26] J. Chen, P. Jung, and H. Klein, J. Nucl. Mater. **258-263**, 1803 (1998).
[27] A. Föhl, R. M. Emrick, and H. D. Carstanjen, Nucl. Instrum. Methods Phys. Res. B **65**, 335 (1992).
[28] W. Puff, A. G. Balogh, and P. Mascher, Mater. Res. Soc. Symp. Proc. **540**, 177 (1999).
[29] F. Gao, W. J. Weber, M. Posselt and V. Belko, Phys. Rev. B **69**, 245205 (2004).
[30] M. V. Rao, J. A. Gardner, P. H. Chi, O. W. Holland, G. Kelner, J. Kretchmer, and M. Ghezzo, J. Appl. Phys. **81**, 6635 (1997).